Check for updates

applied optics

Practical two-dimensional beam steering system using an integrated tunable laser and an optical phased array

Weichao Ma,[1,†] Su Tan,[2,†] Kuankuan Wang,[2] Weihua Guo,[2] Ye Liu,[3] Lianggang Liao,[3] Lianggang Zhou,[3] Jun Zhou,[3] Xin Li,[4] Lei Liang,[4] and Wangzhe Li[1,*]

[1]National Key Laboratory of Microwave Imaging Technology, Aerospace Information Research Institute, Chinese Academy of Sciences, Beijing 100190, China
[2]Wuhan National Laboratory for Optoelectronics & School of Optical and Electronic Information, Huazhong University of Science and Technology, 1037 Luoyu Rd., Wuhan 430074, China
[3]School of Information and Communication Engineering, University of Electronic Science and Technology of China, Chengdu, Sichuan, China
[4]State Key Laboratory of Luminescence and Applications, Changchun Institute of Optics Fine Mechanics and Physics, Chinese Academy of Sciences, Changchun 130033, China
*Corresponding author: wzli@mail.ie.ac.cn

Received 30 July 2020; revised 10 October 2020; accepted 12 October 2020; posted 13 October 2020 (Doc. ID 403314); published 3 November 2020

A practical two-dimensional beam steering solid-state system based on the synthesis of one-dimensional wavelength tuning and a one-dimensional optical phased array is demonstrated and investigated. The system incorporates an integrated multiple-channel-interference widely tunable laser, an integrated 32-channel optical phased array, an offline phase error correction unit, and home-made control electronics. The introduction of the integrated tunable laser avoids the traditional bulky light source fed into the optical phased array, making the architecture promising to be miniaturized. In addition, a calibration method based on particle swarm optimization is proposed and proved to be effective to correct the phase errors existing in the arrayed channels and improve the emitted far-field quality. Other practical aspects, such as high-speed control and cost, are taken into the consideration of the system design as well. Under the control of home-made electronics, the laser exhibits a tuning range of 50 nm with a 44 dB side-mode suppression ratio, and the system presents the characteristics of low divergence (0.63° × 0.58°), high side-lobe suppression ratio (>10 dB), and high-speed response (<10 μs time constant) in an aliasing-free sweeping range of 18° × 7°. © 2020 Optical Society of America

https://doi.org/10.1364/AO.403314

1. INTRODUCTION

Two-dimensional (2D) optical beam steering has become a significant technology in a variety of advanced applications, such as light detection and ranging (LIDAR) and free-space optical communication [1–5]. Traditional beam steering systems rely on mechanical rotations and hence suffer from slow sweeping speed and large volume and weight. Over the past decade, a series of techniques, including the vertical-cavity surface-emitting laser (VCSEL) array [6], reflective micro-electro-mechanical system (MEMS) [7], and integrated optical phased array (OPA) [8], have been proposed towards complete solid-state operation to overcome these drawbacks. Integrated OPA stands out as a particularly promising solution for 2D beam steering. It eliminates the mechanical parts by altering the beam direction via controlling the wave front of the light emitted from arrayed optical antennas, featuring fast scanning, high resolution, small footprint, and conformal aperture [9–11].

According to the arrangement of optical antennas, OPA-based 2D beam steering systems can be divided into two strategies: 1) 2D OPA and 2) one-dimensional (1D) OPA in combination with 1D wavelength tuning. For a 2D $N \times N$ OPA, the complexity to manage the phase shifters and metal routing scales rapidly by N^2 [12]; thus it is difficult to a realize narrow beam width by increasing the channel number. New architecture is trialed to reduce the number of phase shifters [13]. In addition, the antenna-to-antenna spacing is limited by the size of beam splitters and phase shifters, usually larger than 10 μm [14], resulting in the aliasing-free steering range of several degrees. Therefore, the demonstrated active 2D OPA is only 8×8 to date [13–15]. As for the second strategy, 2D beam steering is synthetized by 1D OPA and grating diffraction.

Since beam steering in the grating dimension can be realized by changing the diffraction angle upon different wavelengths, the required channel number is reduced to $1 \times N$ dramatically. Thus, the simple structure draws more attention, and studies focusing on larger scale [5,16,17], narrower channel spacing [18], and various platforms [2,9,19–21] have been reported. However, an extra widely tunable laser is required to sweep the beam by wavelength tuning. Previous research has mainly focused on the OPA chips, and the light sources are provided by an external bulky tunable laser, making the 1D OPA technique less convincing as an attractive scheme for a chip-scale system. In addition, the consideration of cost in various applications expects the lasers to be monolithically integrated, simple to fabricate, and available for mass production. For OPA technology, an algorithm is necessary to calibrate the currents or voltages applied to the phase shifters and achieve the desired far field. Due to the random fabrication nonuniformity of waveguide dimensions and material stress, the crosstalk between adjacent phase shifters, and the fan-in structure to converge the emitting elements, the accumulated optical path deviations at the optical antennas distort the far-field pattern and degrade the beam quality. Since the phase error is inevitable, a feedback process is required to pre-distort the channel phases for high-quality beam steering. Control electronics are another important aspect for a practical 2D beam steering system. The speed of the OPA system depends on the response time of driving electronics and phase shifters. Although phase shifters with several nanoseconds of response time have been reported [22], it is particularly expensive and impractical to drive the OPA chip by circuits containing tens to hundreds of channels at such high speed. The OPA system may be limited by the driving electronics rather than the ultimate speed that phase shifters can achieve. For most OPA-based applications, fast control at the microsecond level is usually needed [5,9,11].

In this work, a system consisting of an integrated multi-channel-interference (MCI) laser, a silicon photonic 1D OPA, an offline phase error correction (PEC) unit, and control electronics is demonstrated as a practical scheme for 2D beam steering. The introduction of the MCI laser, which is proposed by our group [23], instead of a bulky instrument makes the architecture more convincing to miniaturize. The laser integrated with a semiconductor optical amplifier (SOA) monolithically only occupies a tiny footprint of 2.5 mm × 0.5 mm, and it is capable of a wide tuning range (>50 nm), a high side-mode suppression ratio (SMSR, >44 dB), and >20 mW fiber coupled output power. In addition, a robust and easy to implement PEC algorithm based on particle swarm optimization (PSO) is proposed and proved to be effective for phase calibration and beam quality improvement. After the PEC process, the 32-channel 1D OPA fed by the MCI laser is able to steer the optical beam in a range of 18° × 7° with <1° beam divergence and >10 dB side-lobe suppression ratio (SLSR). In system design, aspects such as rapid control and cost are taken into consideration as well. Home-made compact electronics are developed to control the system at high speed (<10 µs time constant) and realize dynamic 2D beam steering.

2. PRINCIPLES AND SCHEME

The illustration of an integrated 1D OPA is shown in Fig. 1. Light is coupled into the input waveguide and then divided into N channels through a branch network. There is one phase shifter in each channel to adjust the optical phase. Then the N-channel waveguides converge to a narrow emitting aperture, where light is scattered into free space via optical antennas.

The cross section of an optical antenna is depicted in Fig. 1(b). The grating structure along the waveguide diffracts the light off the chip following the grating equation [19]:

$$\sin\theta = \frac{\lambda}{\Lambda} - n_{\text{eff}}, \tag{1}$$

where θ represents the steering angle in the cross-section plane, λ is the laser wavelength, Λ is the grating period, and n_{eff} is the effective refractive index of the mode propagating in the waveguide. As is described in Eq. (1), θ depends on the laser wavelength so that it is defined as the steering angle in the wavelength dimension. Therefore, a widely tunable laser is required for a 1D OPA to alter the beam direction θ in a large range. The laser source should also be miniaturized considering the volume, power consumption, and cost of the beam steering system.

In the aperture region, the cross section perpendicular to the waveguides is shown in Fig. 1(c). The N-channel optical antennas constitute a 1D array. Adjusting the optical phase in each channel via the phase shifters changes the wave front emitted from the arrayed antennas. Given a certain wavelength, the interfered optical intensity in the far field can be expressed as Eq. (2) in analogy to the radio-frequency phased array theory [24]:

$$\begin{aligned} I(\psi) &= |E(\psi) f(\psi)|^2 \\ &= I_0 \text{Sinc}^2\left[\frac{\pi a \sin(\psi)}{\lambda}\right] \\ &\quad \times \left|\sum_{i=1}^{N} \exp\left(-j\varphi_i + j\frac{2\pi}{\lambda} x_i \sin(\psi)\right)\right|^2. \end{aligned} \tag{2}$$

Here $I(\psi)$ is the far-field intensity distribution in the phase dimension and I_0 is a constant. E represents the electromagnetic radiation of a single optical antenna in the far field. It is related to the waveguide width a and determines the profile

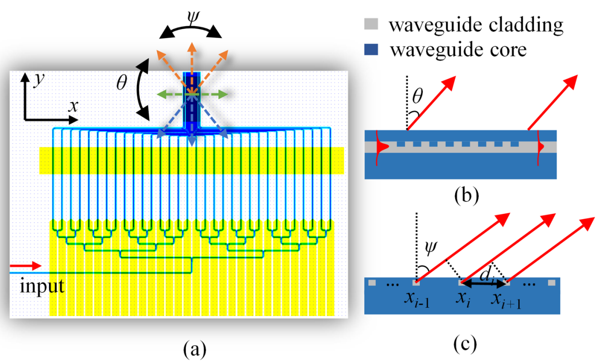

Fig. 1. Illustration of an integrated 1D OPA. (a) Top view of an integrated 1D OPA. (b) Cross section of an optical antenna. (c) Cross section of the aperture region perpendicular to the waveguides.

of the far-field intensity I. f is the array factor that reflects the configuration of the phased array, including the phase φ_i and position x_i of each antenna. Beam forming can be realized by controlling the phase gradient of the array. The emitted beam is oriented at ψ_0 when the phase difference of adjacent antennas satisfies Eq. (3), that is, the emitted optical field interferes constructively in the direction of ψ_0:

$$\Delta\varphi = \varphi_i - \varphi_{i+1} = \frac{2\pi d_i}{\lambda}\sin(\psi_0). \tag{3}$$

An antenna array with uniform spacing of d is analyzed here to clarify the critical characteristics of OPA intuitively in analytical form. By substituting Eq. (3) into Eq. (2), the far-field intensity distribution can be expressed as

$$I(\psi) = I_0 \mathrm{Sinc}^2\left(\frac{\pi a \sin\psi}{\lambda}\right)\cdot\frac{\mathrm{Sin}^2\left[\frac{N\pi d(\sin\psi - \sin\psi_0)}{\lambda}\right]}{\mathrm{Sin}^2\left[\frac{\pi d(\sin\psi - \sin\psi_0)}{\lambda}\right]}. \tag{4}$$

Since optical coupling occurs as the spacing between two waveguides narrows, it is difficult to achieve spacing narrower than a half wavelength. As a result, high-order lobes appear at ψ_m according to Eq. (5):

$$\psi_m = \arcsin\left(\sin\psi_0 + m\frac{\lambda}{d}\right), \quad m = \pm 1, \ \pm 2 \ldots |m| \le \frac{2d}{\lambda}. \tag{5}$$

As the beam steers, the coverage of the high-order lobes may overlap with that of the main-lobe, resulting in interference. The aliasing-free sweeping range $\Delta\psi$ is determined by the location of ± 1-order lobes and can be approximated as

$$\mathrm{Sin}\Delta\psi \approx \frac{\lambda}{d}. \tag{6}$$

Besides the high-order lobes, there are also some small side-lobes in the vicinity of the main-lobe. SLSR is adopted to evaluate the ratio of the main-lobe intensity to the highest side-lobe in the aliasing-free steering range. In addition, beam divergence is used to evaluate the width of the emitted beam. Following most of the literature, beam divergence is defined as the full width at half maximum (FWHM) of the main-lobe intensity and can be calculated from Eq. (4). It is indicated that increasing the number of OPA channels leads to narrower beam divergence:

$$\psi_{\mathrm{FWHM}} \propto \frac{\lambda}{Nd}. \tag{7}$$

SLSR and beam divergence are used to evaluate the beam quality, and they influence the performance of various applications. Taking LIDAR for example, high SLSR is able to detect a weak reflection target near a strong one, while narrow beam divergence obtains high resolution.

The analysis above is based on the precondition that the near-field phases emitted from the arrayed antennas satisfy the relationship of Eq. (3). However, there exists phase deviation in each OPA channel due to the inevitable nonuniformity, including waveguide dimensions, internal stress, electrical properties, and crosstalk. Therefore, it is difficult to obtain an emitted beam with desired directionality and beam quality in an open loop system. Far-field characterization and the PEC algorithm are required to compensate these random phase deviations. In addition, control electronics are also needed to drive the system at high speed.

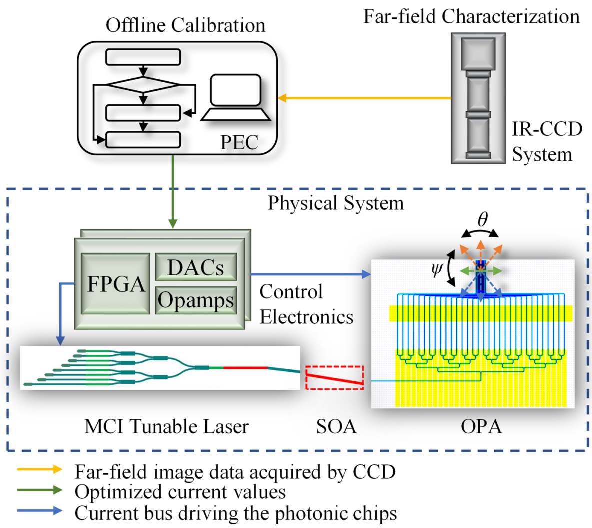

Fig. 2. Scheme of the proposed two-dimensional beam steering system based on integrated MCI laser and OPA.

According to the requirement of 1D OPA for a widely tunable laser, PEC feedback, and fast control, a scalable 2D beam steering architecture is proposed and illustrated in Fig. 2, consisting of an integrated MCI tunable laser, a SOA, an OPA, control electronics, far-field characterization, and offline calibration units. The MCI laser, proposed by our group in previous works for wavelength division multiplexing systems [23], features a small footprint and a wide tuning range. The output of the MCI laser is fed into the SOA to boost the optical power and then coupled into the OPA. Increasing the output power supports the system for longer distance applications. Typically, the optical power requirement of frequency-modulation continuous wave (FMCW) coherent detection is tens of milliwatts [9]. Compared with the mature erbium-doped fiber amplifier (EDFA) technology, SOA may be more preferred here in terms of size, weight, power consumption, and cost. In order to leverage the technology of optical fiber communication, the photonic chips can be designed at the C or L band on the indium phosphide (InP) platform for the MCI laser and SOA, and the silicon photonic platform for the OPA. Tuning the laser wavelength alters the diffraction angle θ by the grating etched in the OPA aperture, while the phase adjustment of the 1D OPA steers the beam in the orthogonal direction ψ. Consequently, the combination of independent wavelength tuning and phase adjustment synthetizes 2D beam steering.

The MCI laser and the OPA chip are controlled by the home-made electronics, providing currents injected into the wavelength selective unit in the MCI laser and the phase shifters in the OPA chip. The far-field pattern emitted from the OPA is monitored by an infrared charge coupled device (IR-CCD) system. The recorded intensity distribution is sent to a computer and characterized. Then a PEC program, accomplished by PSO in the work, is carried out to update the output of control electronics. Under the feedback of this offline calibration, the pre-distorted currents are set to eliminate the phase errors in the OPA chip. The beam quality is optimized, and the corresponding current values are saved in a look-up table (LUT). Afterwards, the offline calibration part is removed and the physical system can steer the optical beam independently via loading the pre-stored values.

3. COMPONENTS

A. MCI Laser

The proposed integrated widely tunable laser is realized by a MCI structure on an InP platform, and the microscope picture is given in Fig. 3(a). The MCI laser consists of a gain section, a 1×8 splitter network, and eight-channel phase arms with different lengths. Seven cascaded 1×2 multimode interference (MMI) couplers constitute the splitter network pitch-matched with the eight channels. The resonant cavity is formed between the one-port multimode interference reflectors (MIRs) and the two-port MIR. In the cavity, mode selection is realized by the optical length differences between the eight channels. The splitter network and channels can be regarded as a frequency selective unit. The adjustment of the current-injection phase shifter in each channel creates constructive interference at the desired wavelength and suppresses the reflection in the other range. The SOA illustrated in Fig. 2 is integrated together with the MCI laser in front of the two-port MIR to promote the output power. The SOA waveguide is at a 7° angle with respect to the normal of the cleaved facet. The cleaved facet is further anti-reflection coated to avoid laser instability caused by unintentional facet reflection. Details about the principles, epitaxial layers, fabrication process, and wavelength characterization can be found in [23,25].

The active and passive integration of the laser source is implemented by an offset quantum well technique. The fabrication process is similar to a DFB laser, which operates at fixed wavelength and is widely used in optical fiber communication. In addition, the footprint of the laser and SOA is only 2.5 mm × 0.5 mm. These characteristics indicate that the MCI laser is compatible with the existing microfabrication technology, available to be mass-produced with low cost. It might be an ideal light source for OPA-based applications.

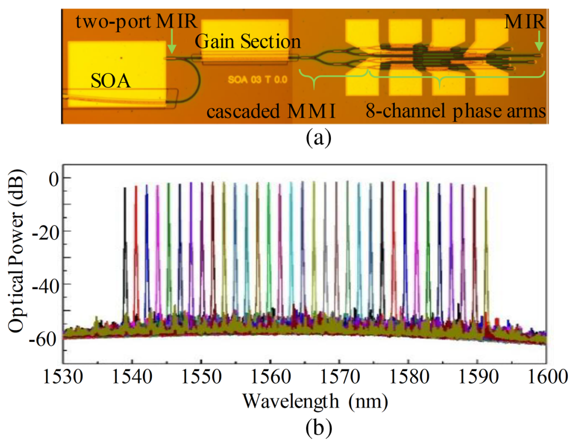

Fig. 3. (a) Microscope image of the MCI widely tunable laser. (b) Superimposed optical spectra of the laser at different lasing wavelengths.

The tuning performance of the MCI laser is characterized and shown in Fig. 3(b). The laser frequency is tuned by 200 GHz steps, and the optical spectra are superimposed. The wavelength interval is able to be characterized coarser or finer, which actually depends on the demand of beam steering resolution in the wavelength dimension. Each wavelength corresponds to a set of eight current values injected to the phase arms. A wavelength tuning span of 53 nm with SMSR higher than 44 dB is achieved, showing larger range than the SG-DBR [26] laser or hybrid laser [20]. The tuning ability is limited by the nonuniform gain of multiple quantum wells. Adjusting the wavelength further beyond the margin will result in lasing of unwanted modes around the gain peak. According to Eq. (1), a steering range of 7.4° can be expected via tuning the MCI laser. The laser is amplified by the monolithically integrated SOA biased at 220 mA, and the fiber coupled power is higher than 13 dBm within 2 dB flatness.

B. Optical Phased Array

The OPA studied in the experiment is designed and fabricated on 500 nm silicon-on-insulator (SOI) wafers. The microscope image and scanning electron microscope pictures of the OPA are shown in Figs. 4(a)–4(d). The edge coupled input waveguide is split into 32 thermo-optics phase shifters through the cascaded 1×2 MMI couplers; then the waveguides converge into the emitting aperture containing 32 optical antennas. Limited by the photolithography resolution in our lab, the waveguide width and minimum element spacing (center to center) are set as 1.5 µm and 4.5 µm, respectively. The phase shifters use the thermo-optics effect to adjust the refractive index of the waveguide and generate a phase gradient for beam steering. The heaters are formed by depositing Au/Ti on the silica cladding and the lift-off process. The measured resistances are around 250 Ω, and 31.5 mW thermal power can induce a 2π phase shift. Independent electrode routing is adopted to allow flexible and accurate phase calibration for each channel in comparison with the grouped type [27]. In order to mitigate the thermal crosstalk, the spacing between phase shifters is increased to 100 µm, an order larger than that of the elements in the aperture region. The bending radius of the fan-in and fan-out structure in the OPA is designed as 60 µm to avoid unwanted coupling to high-order modes. The OPA aperture uses gratings as optical antennas to diffract light into free space. The gratings are shown in Fig. 4(d) with 476 nm pitch and 50% duty cycle. The optical antennas are designed with 50 nm etching depth and 500 µm length to diffract 90% light out of the waveguide. The buried oxide layer is optimized as 1.3 µm, similar to the process described in [28], to realize 60%–70% upward diffraction efficiency.

The far-field intensity emitted by the OPA in the phase dimension is simulated based on Eq. (2) and shown in Fig. 4(e). Most intervals of the optical antennas are 4.5 µm, namely the minimum spacing allowed, except that the six spacings on both sides adopt a nonuniform distribution from 5.2 µm to 17 µm, which promotes the SLSR compared with the case of a uniform distribution. The 4.5 µm antenna spacing corresponds

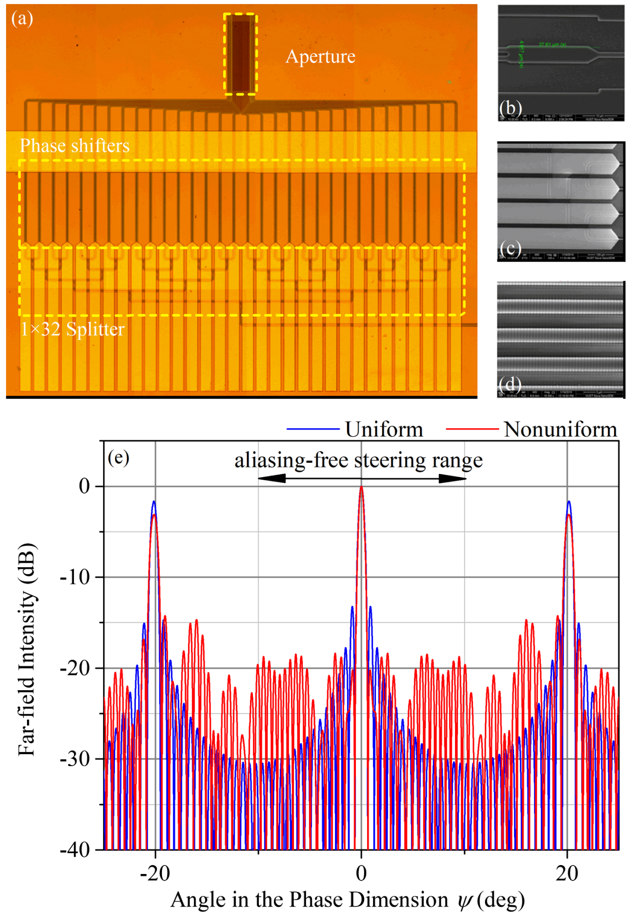

Fig. 4. (a) Microscope image of the OPA chip and scanning electron microscope (SEM) pictures of (b) MMI, (c) electrodes of phase shifters, and (d) gratings cladded by SiO_2 in the aperture region. (e) Simulated intensity distribution of far field in the phase dimension (blue line, uniform antennas; red line, nonuniform antennas).

to the first-order lobes located around ±20°, revealing a ±10° aliasing-free sweeping range. It should be noted that reducing the optical antenna pitch to subwavelength and increasing the element scale is beneficial to achieving a wider sweeping range and a narrower beam width. These aspects can be implemented via mature silicon photonic technology with high lithography resolution provided by institutes or foundries such as IMEC, AMF, or AIM [9,29]. Since this work focuses on system architecture, the OPA fabricated in the lab is utilized. However, the key considerations have been clarified above and the performance can be improved further accordingly.

C. Control Electronics

The photonic chips are driven by the home-made electronics to tune the laser wavelength and introduce phase shifts for optical beam forming. The corresponding printed circuit boards (PCBs) are shown in Fig. 5. For LIDAR application, sweeping at the speed of several microseconds is required to promise real-time imaging. However, there exists a trade-off for digital–analog converters (DACs) between output current and response speed. In addition, for a practical system, the response time may

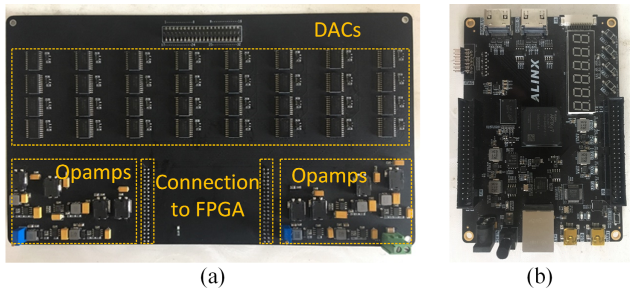

Fig. 5. (a) PCB electronics driving the phase shifters of OPA. (b) FPGA board controlling the physical system.

be limited by the interaction between FPGA and DACs instead of the OPA device [5]. Cost should be also taken into consideration as it scales with the number of OPA channels. Therefore, the DACs (TLV5619) are followed by the operator amplifiers (Opamp, AD8065) in the design to provide enough current for a 2π phase shift at high speed. For the OPA scaled to the order of ∼1000 channels, integrated CMOS circuits and 3D packaging technology [30] can be utilized to realize a compact system and high-density electrode connection.

The electronics driving the MCI laser are similar to those for the OPA, except that the channel number is reduced to eight and the high-output DACs (ADN8810) are utilized to inject current into the active regions. An FPGA (Xilinx Artix-7) is employed to control the physical system, including the feedback from offline calibration and online beam steering. The optimized current sets ($\boldsymbol{I}_L$, $\boldsymbol{I}_{\mathbf{OPA}}$) of the MCI laser $\boldsymbol{I}_L$ and the OPA $\boldsymbol{I}_{\mathbf{OPA}}$, corresponding to various steering angles (ψ, θ), are recorded in a LUT. Then the current values are loaded and set to the photonic chips by the electronics for dynamic 2D beam steering.

4. EXPERIMENTS AND RESULTS

A. Experimental Setup

The schematic diagram and experimental setup of the 2D beam steering system are depicted in Fig. 6. The output of the monolithically integrated MCI laser and SOA is fed into the OPA chip, and a polarization control (PC, Thorlabs FPC562) is inserted to guarantee polarization matching. For the convenience of joint testing and enhancing the robustness, the photonic chips are packaged at different levels. As is shown in Figs. 6(c) and 6(d), the laser source is soldered to a sub mount with a temperature sensor and Peltier cooler, and then packaged in a 16-pin butterfly shell, while the OPA is die-attached to a PCB and wire-bonded to a series of pads. They are connected to the control electronics in Figs. 6(e) and 6(f) through Dupont lines. The MCI laser and the OPA are stabilized at 20°C and 25°C, respectively, by TEC controllers (LDT-5525B). A visible CCD (VIS-CCD) system is employed to monitor the coupling between the lensed fiber and the OPA input waveguide using red light; then it is switched to the IR-CCD (ARTCAM-008TNIR) system aligned with the OPA aperture to characterize the emitted beam quality. The emitted field is converted to far field by lens optics similar to those in [2,20]. The computer analyzes

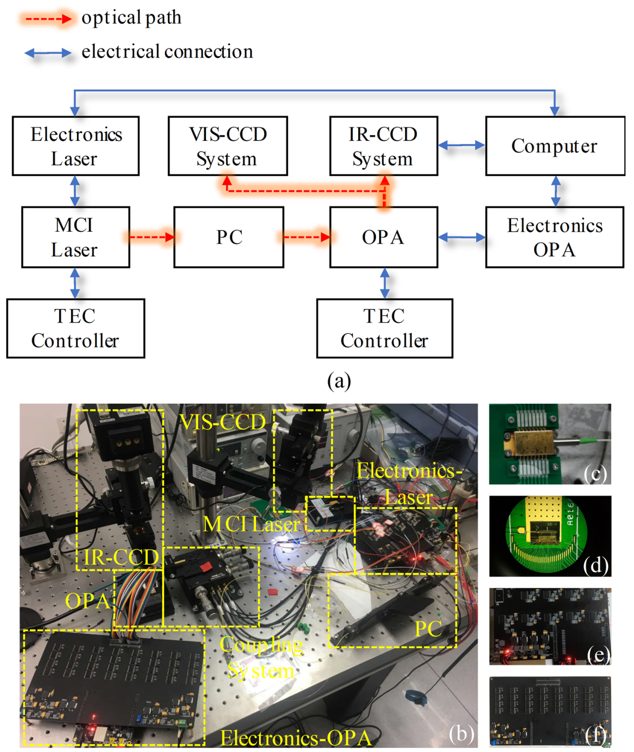

Fig. 6. (a) Schematic diagram and (b) experimental setup of two-dimensional beam steering system based on integrated laser and OPA. (c) MCI laser packaged in a 16-pin butterfly shell. (d) OPA chip soldered on PCB and wire-bonded to external pads. Control electronics for (e) MCI laser and (f) OPA.

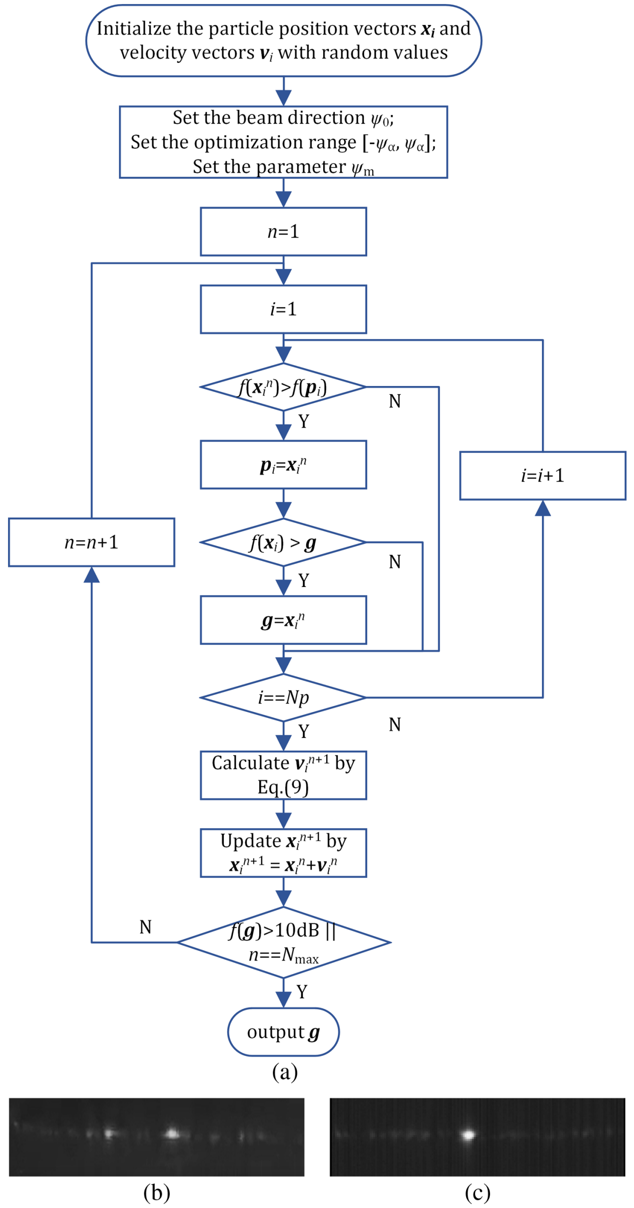

Fig. 7. (a) Flow chart of PEC process. Monitored far-field pattern by IR-CCD (b) before and (c) after the PEC process.

the far-field data acquired from the IR-CCD system and conducts the PEC algorithm to provide feedback to the control electronics.

It should be noted that the 1.5 μm wide waveguide in the OPA supports high-order modes, so the excitation of these modes needs to be avoided during the experiment. The MMI couplers and optical antennas in the OPA are designed based on the fundamental TE mode. Therefore, for the high-order modes, the transmission of the MMI coupler is reduced and the beam is diffracted at unwanted angles due to different effective refractive index according to Eq. (1). Through the feedback of intensity and diffraction angle monitored by the infrared CCD, the polarization controller is adjusted to avoid the excitation of the TM mode and the position of the lensed fiber is tuned carefully to mitigate the appearance of the high-order TE mode.

B. Phase Error Correction

For the integrated OPA technology, there exist phase deviations in the arrayed channels induced by imperfect fabrication, heat crosstalk, and unequal waveguide routings. These deviations cannot be avoided due to the randomness. As a result, it is difficult to obtain a desired far-field distribution by applying the current of multiple phase shifters according to the simulated values. Therefore, PEC feedback is necessary to optimize the far-field characteristics, including directionality, beam divergence, and SLSR. The process to improve the far-field quality can be regarded as a nonlinear optimization problem, that is, finding the solution of N-channel currents that maximizes the objective function evaluating the beam quality. In this work, this process is realized by the PSO method, which mimics swarm behavior such as bird flocking and has the advantages of a simple concept, easy implementation, and robustness to control parameters [31–33].

The flow chart of the proposed PEC method is shown in Fig. 7(a). During the algorithm implementation, the current values injected into the phase shifters of the OPA form a N-dimensional ($N = 32$) vector $\boldsymbol{x}$ called the position of the particle, while the variations of these current values after each iteration form vector $\boldsymbol{v}$, representing the velocity of the particle. At the beginning, the positions and corresponding velocity vectors of N_p ($N_p = 7$) particles are initialized randomly in a 0–12 mA range, which is large enough to generate a 2π phase shift. Then the beam quality obtained by each particle is calculated as fitness, which is defined as

$$f(\boldsymbol{x}) = \frac{I|_{\psi=\psi_0}}{I|_{\psi_m<|\psi-\psi_0|<\psi_a}}, \tag{8}$$

namely, the ratio of far-field intensity at ψ_0 to the maximum intensity in the range of $\psi_m < |\psi - \psi_0| < \psi_a$. Here, ψ_m constrains the main-lobe width and $\psi_\alpha (\psi_\alpha = 10°)$ is half of the aliasing-free steering angle. A smaller ψ_m parameter contributes to narrower beam divergence, and it can be set as approximately twice the theoretical beam divergence according to our experimental experience. The maximization optimization of $f(\boldsymbol{x})$ can realize an emitted beam oriented at ψ_0 with high SLSR.

During the iteration to improve the far-field beam quality, each particle $\boldsymbol{x}_i^n$ is updated by $\boldsymbol{x}_i^{n+1} = \boldsymbol{x}_i^n + \boldsymbol{v}_i^n$ at the nth loop. The velocity $\boldsymbol{v}_i^n$ is derived via the following relationship:

$$\boldsymbol{v}_i^n = \omega \times \boldsymbol{v}_i^n + c_1 \times r_1 \times (\boldsymbol{p}_i^n - \boldsymbol{x}_i^n) + c_2 \times r_2 \times (\boldsymbol{g}^n - \boldsymbol{x}_i^n). \tag{9}$$

ω is the inertia weight, which is used to balance the global and local search ability [33]. It decreases linearly from 0.9 to 0.4 as the iteration time increases. c_1 and c_2 are acceleration constants and set as 2. r_1 and r_2 are random variables between [0,1]. The maximum magnitude of the particle's velocity on each dimension is limited to [−4 mA, 4 mA]. Any value that exceeds the limit is clamped to the boundary. The evolutionary process is terminated when the fitness is larger than 10 dB or $N_{\max}$ iterations ($N_{\max} = 200$) are finished.

An instance of the improvement of the far-field pattern is recorded by the IR-CCD and shown in Figs. 7(b) and 7(c). The light spot of the original far field disperses in the phase dimension, indicating large beam width. In addition, a strong side-lobe exists on the left side of the main-lobe and hence degrades the SLSR. During the experiment, it is also found that it is difficult to control the orientation of the formed beam flexibly and accurately. After the automatic PEC process accomplished via the PSO algorithm, the far field converges to a single spot with promoted beam quality at the desired orientation.

The proposed PEC method is also valid for large-scale OPA, and it is demonstrated in Fig. 8. The far field of an OPA with 1024 channels is simulated according to Eq. (2). For the initial state, random phase error values with a standard deviation of $\pi/2$ are added to ideal channels and the SLSR is only 3.2 dB. Since the channel number is enlarged significantly, the particle number is also increased to $N_p = 50$. After 200 iterations, the SLSR of the optimized far field is improved to 13.5 dB and the beam divergence is 0.017°.

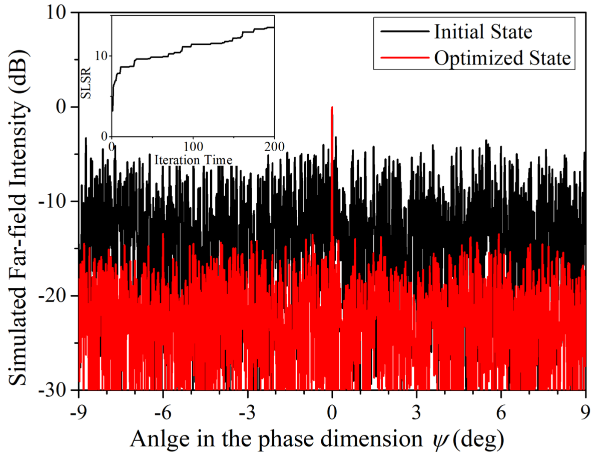

Fig. 8. Simulated far-field optimization process conducted by the PSO method for an OPA with 1024 channels. Inset: improvement of SLSR as the iteration proceeds.

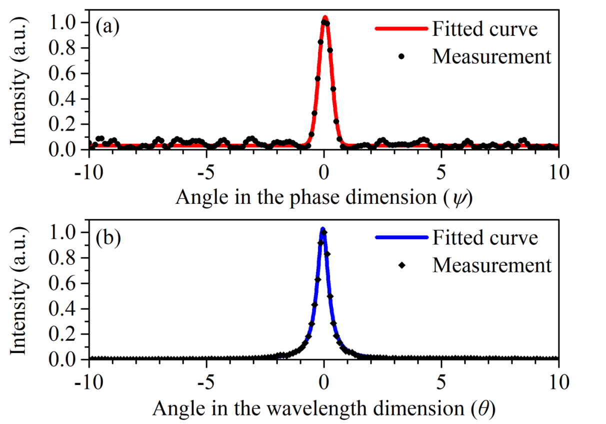

Fig. 9. Far-field slices through spot center in (a) phase dimension and (b) wavelength dimension.

C. Quality of Far Field

The quality of the emitted far field is recorded by the IR-CCD system and analyzed in terms of beam divergence and SLSR. During the measurement, the exposure time of the IR-CCD is controlled carefully to make sure that the responsivity is in the linear region, or saturation will result in overestimation of the far-field width. The beam divergences in both dimensions are extracted by the orthogonal slices through the center of the main-lobe and given in Fig. 9.

For the OPA, the antenna pitches at both ends of the aperture are nonuniform. In addition, there may exist some residual deviations from ideal phase differences in the 32 channels for beam forming. Therefore, the far-field intensity distribution in the phase dimension tends to be Gaussian and the fitted beam divergence is 0.63°, close to the designed value of 0.52°. According to the OPA theory, the beam width is in reverse proportion to the channel number. Taking the advantage of a mature silicon photonic platform, the scale can be expanded to 512 or larger [5,16,34]. 512 elements will lead to a predicted resolution of 0.039°, which is narrow enough for autonomous or assistant driving applications. It should be noted that in order to characterize the far-field quality of larger scale OPA, the IR-CCD system should also be modified with a larger pixel number and a smaller pixel size to provide enough resolution. As for the grating antenna, the diffracted near field decays exponentially along the waveguide due to the uniform grating structure. Hence the far field should present a Lorentzian line shape according to the Fourier transform. The extracted beam divergence is 0.58° in the wavelength dimension, sufficient for LIDAR application since the height information usually has a smaller impact on

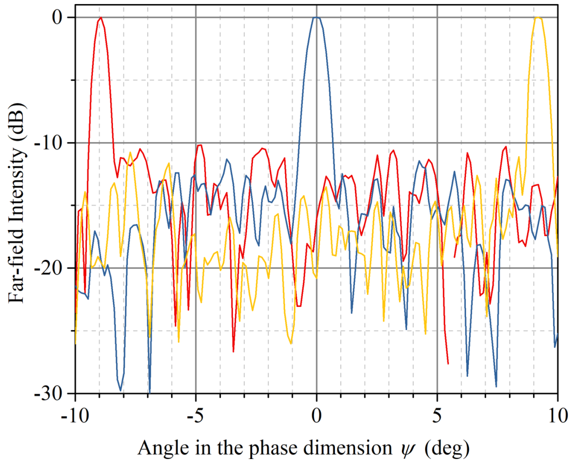

Fig. 10. Far-field intensity slices in the phase dimension at angles of $-9°$, $0°$, and $9°$.

target recognition [9]. Since there are no peaks residing in the wings of the main-lobe in Fig. 9(b), the excitation of high-order modes in the 1.5 µm wide OPA waveguide can be neglected.

The optical antennas employ a second-order grating with a period shorter than half-wavelength in air, so there is not any side-lobe in the wavelength dimension. The SLSR only needs to be analyzed in the phase dimension. Figure 10 shows the far-field intensity distribution when the beam is steered at the leftmost, middle, and rightmost angles. Each curve is normalized to the maximal intensity. Thanks to the PEC process, the SLSRs remain below 10 dB. As is presented in Refs. [17,28], the absence of PEC or an unoptimized algorithm only achieves an SLSR of several decibels, degraded far from the design. The high SLSR indicates that the proposed approach calibrates the phase errors in different channels effectively.

D. Two-Dimensional Beam Steering

The integrated laser source, OPA, and control electronics constitute the physical part of the beam steering system. After the PEC process, the offline calibration part is removed and the physical part is able to conduct dynamic 2D beam steering by loading the data stored in the LUT. The far fields in different directions are monitored by the IR-CCD and shown in Fig. 11. The white frame marks the aliasing-free scanning region. Benefiting from the PEC algorithm, the far fields exhibit a single spot with low divergence and high SLSR. A steering range of 18° in the ψ dimension is obtained by altering the phase gradient of the phase shifters in the OPA chip, and a steering range of 7° in the θ dimension is achieved by tuning the laser wavelength over a 50 nm span with an efficiency of 0.14 deg/nm. A wider steering range can be realized by expanding the laser tuning range, such as utilizing two MCI lasers to cover the entire C and L bands.

The speed of the OPA chip is characterized by an asymmetric Mach–Zehnder interference (AMZI) structure using the same phase shifters as the OPA. As the current injected into the phase shifter is adjusted, the output of the AMZI is fed into a photodetector (PD) monitored by an oscilloscope. The result is given in Fig. 12(a). When the current changes by the green square

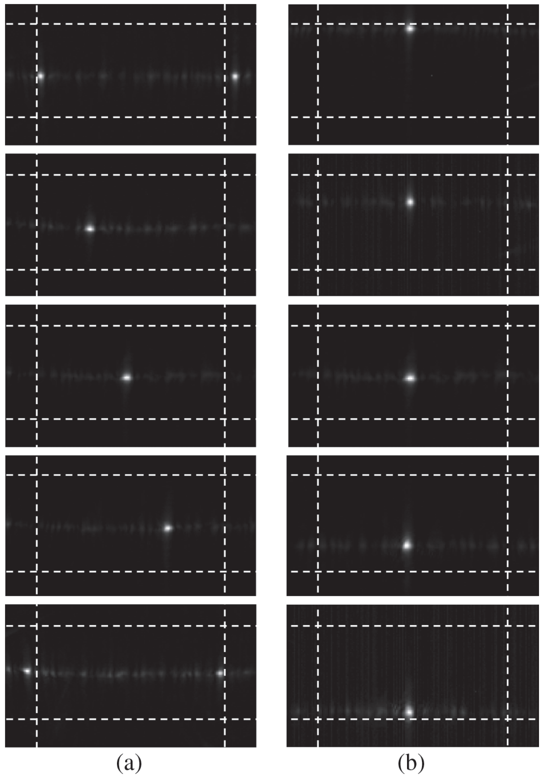

Fig. 11. Two-dimensional beam steering recorded by IR-CCD. (a) Far fields at $\psi = -9°$, $\psi = -4°$, $\psi = 0°$, $\psi = 4°$, and $\psi = 9°$. (b) Far fields at $\theta = 3.5°$, $\theta = 1.7°$, $\theta = 0°$, $\theta = -1.7°$, and $\theta = -3.5°$.

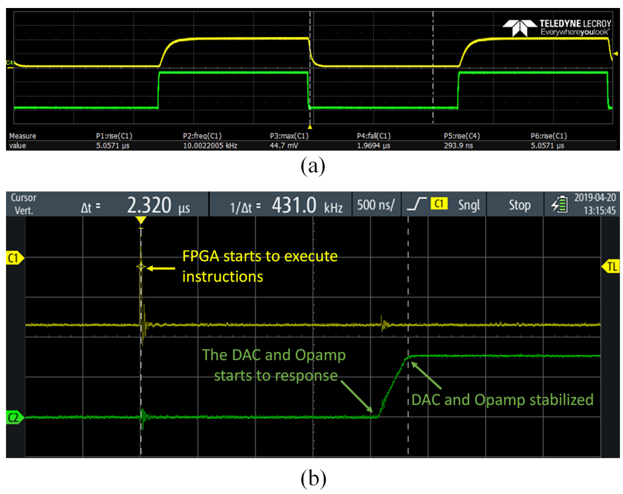

Fig. 12. (a) Response of AMZI (yellow line) upon the square wave (green line) added on one arm of AMZI. (b) Interaction sequence of FPGA with DACs and Opamps.

wave between 0 and I_π, the output power of the AMZI switches between the maximal and minimal values, recorded as the yellow line. The time constants of the rising and falling edges of the yellow line are 5.06 µs and 1.97 µs, respectively. The interaction time of the FPGA with the DACs and Opamps is also measured and depicted in Fig. 12(b). The interaction limited response time is 2.07 μs. The fast response times of the phase shifters and the electronic circuits (<10 μs in total) demonstrate the ability of high-speed beam steering.

5. CONCLUSION

In conclusion, a practical 2D beam steering scheme based on an integrated MCI laser and OPA is demonstrated. The introduced MCI laser features a wide tuning range (>50 nm), high SMSR (>44 dB), and a small footprint, satisfying the requirements of a miniaturized solid-state steering system. A PEC process implemented by PSO is proposed to correct phase errors in the OPA channels and improve the far-field quality effectively. Under the control of home-made electronics, which weighs the driving capability and response time, the system is able to conduct dynamic 2D beam steering over an aliasing-free range of $18^\circ \times 7^\circ$ with low divergence ($0.63^\circ \times 0.58^\circ$ for 32 channels), high SLSR (>10 dB), and fast response (<10 μs time constant). We will focus on expanding the steering range and pursue a higher integration level in future work.

Funding. National Key Research and Development Program of China (2019YFB2203300, 2019YFB2203302); National Natural Science Foundation of China (61690191, 61701476); Key Research Program of Frontier Sciences, CAS (ZDBS-LY-JSC016).

Disclosures. The authors declare that there are no conflicts of interest.

[†]These authors contributed equally to this paper.

REFERENCES

1. J.-W. Shi, J.-I. Guo, M. Kagami, P. Suni, and O. Ziemann, "Photonic technologies for autonomous cars: feature introduction," Opt. Express **27**, 7627–7628 (2019).
2. W. Xie, T. Komljenovic, J. Huang, M. Tran, M. Davenport, A. Torres, P. Pintus, and J. Bowers, "Heterogeneous silicon photonics sensing for autonomous cars," Opt. Express **27**, 3642–3663 (2019).
3. S. Royo and M. Ballesta-Garcia, "An overview of lidar imaging systems for autonomous vehicles," Appl. Sci. **9**, 4093 (2019).
4. C. Pulikkaseril and S. Lam, "Laser eyes for driverless cars: the road to automotive LIDAR," in *Optical Fiber Communication Conference (OFC)* (OSA, 2019), paper Tu3D.2.
5. C. V. Poulton, M. J. Byrd, P. Russo, E. Timurdogan, M. Khandaker, D. Vermeulen, and M. R. Watts, "Long-range LiDAR and free-space data communication with high-performance optical phased arrays," IEEE J. Sel. Top. Quantum Electron. **25**, 1–8 (2019).
6. K. Sayyah, O. Efimov, P. Patterson, J. Schaffner, C. White, J.-F. Seurin, G. Xu, and A. Miglo, "Two-dimensional pseudo-random optical phased array based on tandem optical injection locking of vertical cavity surface emitting lasers," Opt. Express **23**, 19405–19416 (2015).
7. B.-W. Yoo, M. Megens, T. Chan, T. Sun, W. Yang, C. J. Chang-Hasnain, D. A. Horsley, and M. C. Wu, "Optical phased array using high contrast gratings for two dimensional beamforming and beamsteering," Opt. Express **21**, 12238 (2013).
8. K. Van Acoleyen, W. Bogaerts, J. Jágerská, N. Le Thomas, R. Houdré, and R. Baets, "Off-chip beam steering with a one-dimensional optical phased array on silicon-on-insulator," Opt. Lett. **34**, 1477 (2009).
9. X. Sun, L. Zhang, Q. Zhang, and W. Zhang, "Si photonics for practical LiDAR solutions," Appl. Sci. **9**, 4225 (2019).
10. P. F. McManamon and A. Ataei, "Progress and opportunities in the development of nonmechanical beam steering for electro-optical systems," Opt. Eng. **58**, 120901 (2019).
11. M. J. R. Heck, "Highly integrated optical phased arrays: photonic integrated circuits for optical beam shaping and beam steering," Nanophotonics **6**, 93–107 (2017).
12. J. Sun, E. Timurdogan, A. Yaacobi, E. S. Hosseini, and M. R. Watts, "Large-scale nanophotonic phased array," Nature **493**, 195–199 (2013).
13. F. Ashtiani and F. Aflatouni, "N × N optical phased array with 2N phase shifters," Opt. Express **27**, 27183–27190 (2019).
14. J. Sun, E. Timurdogan, A. Yaacobi, Z. Su, E. S. Hosseini, D. B. Cole, and M. R. Watts, "Large-scale silicon photonic circuits for optical phased arrays," IEEE J. Sel. Top. Quantum Electron. **20**, 264–278 (2014).
15. H. Abediasl and H. Hashemi, "Monolithic optical phased-array transceiver in a standard SOI CMOS process," Opt. Express **23**, 6509–6519 (2015).
16. C. V. Poulton, M. J. Byrd, M. Raval, Z. Su, N. Li, E. Timurdogan, D. Coolbaugh, D. Vermeulen, and M. R. Watts, "Large-scale silicon nitride nanophotonic phased arrays at infrared and visible wavelengths," Opt. Lett. **42**, 21–24 (2017).
17. S. A. Miller, Y.-C. Chang, C. T. Phare, M. C. Shin, M. Zadka, S. P. Roberts, B. Stern, X. Ji, A. Mohanty, O. A. Jimenez Gordillo, U. D. Dave, and M. Lipson, "Large-scale optical phased array using a low-power multi-pass silicon photonic platform," Optica **7**, 3–6 (2020).
18. C. T. Phare, M. C. Shin, J. Sharma, S. Ahasan, H. Krishnaswamy, and M. Lipson, "Silicon optical phased array with grating lobe-free beam formation over 180 degree field of view," in *Conference on Lasers and Electro-Optics* (OSA, 2018), paper SM3I.2.
19. W. Guo, P. R. A. Binetti, C. Althouse, M. L. Masanovic, H. P. M. M. Ambrosius, L. A. Johansson, and L. A. Coldren, "Two-dimensional optical beam steering with InP-based photonic integrated circuits," IEEE J. Sel. Top. Quantum Electron. **19**, 8500508 (2013).
20. J. C. Hulme, J. K. Doylend, M. J. R. Heck, J. D. Peters, M. L. Davenport, J. T. Bovington, L. A. Coldren, and J. E. Bowers, "Fully integrated hybrid silicon two dimensional beam scanner," Opt. Express **23**, 5861–5864 (2015).
21. N. A. Tyler, D. Fowler, S. Malhouitre, S. Garcia, P. Grosse, W. Rabaud, and B. Szelag, "SiN integrated optical phased arrays for two-dimensional beam steering at a single near-infrared wavelength," Opt. Express **27**, 5851–5858 (2019).
22. C. Zhao, H. Zhang, Z. Zheng, C. Peng, and W. Hu, "Silicon optical-phased-array prototypes using electro-optical phase shifters," in *Conference on Lasers and Electro-Optics (CLEO)* (2017), pp. 1–2.
23. Q. Chen, X. Ma, W. Sun, Y. Liu, G. Liu, G. Zhao, Q. Lu, and W. Guo, "Demonstration of multi-channel interference widely tunable semiconductor laser," IEEE Photon. Technol. Lett. **28**, 2862–2865 (2016).
24. R. L. Haupt, "Array factor analysis," in *Antenna Arrays: A Computational Approach* (Wiley, 2010), Chap. 2, sec. 2.1, pp. 45–55.
25. Q. Chen, G. Liu, Q. Lu, and W. Guo, "Optimization algorithm based characterization scheme for tunable semiconductor lasers," Opt. Express **24**, 20982–20992 (2016).
26. P. J. M. Suni and J. Bowers, "Photonic integrated circuit FMCW lidar on a chip," in *19th Coherent Laser Radar Conference* (2018), p. 4.
27. C. V. Poulton, A. Yaacobi, D. B. Cole, M. J. Byrd, M. Raval, D. Vermeulen, and M. R. Watts, "Coherent solid-state LIDAR with silicon photonic optical phased arrays," Opt. Lett. **42**, 4091–4094 (2017).
28. Y. Zhang, Y.-C. Ling, K. Zhang, C. Gentry, D. Sadighi, G. Whaley, J. Colosimo, P. Suni, and S. J. B. Yoo, "Sub-wavelength-pitch silicon-photonic optical phased array for large field-of-regard coherent optical beam steering," Opt. Express **27**, 1929–1940 (2019).
29. E. Timurdogan, Z. Su, C. V. Poulton, M. J. Byrd, S. Xin, R. Shiue, B. R. Moss, E. S. Hosseini, and M. R. Watts, "AIM process design kit (AIMPDKv2.0): silicon photonics passive and active component libraries on a 300 mm wafer," in *Optical Fiber Communications Conference and Exposition (OFC)* (2018), pp. 1–3.
30. Y. Yang, M. Yu, Q. Fang, J. Song, X. Tu, P. G.-Q. Lo, and Rusli, "3D silicon photonics packaging based on TSV interposer for high density

on-board optics module," in *IEEE 66th Electronic Components and Technology Conference (ECTC)* (2016), pp. 483–489.
31. J. Kennedy and R. C. Eberhart, "Particle swarm optimization," in *IEEE International Conference on Neural Networks* (1995), pp. 1942–1948.
32. Y. Shi and R. Eberhart, "A modified particle swarm optimizer," in *IEEE International Conference on Evolutionary Computation Proceedings. IEEE World Congress on Computational Intelligence (Cat. No.98TH8360)* (IEEE, 1998), pp. 69–73.
33. J. J. Liang, A. K. Qin, P. N. Suganthan, and S. Baskar, "Comprehensive learning particle swarm optimizer for global optimization of multimodal functions," IEEE Trans. Evol. Comput. **10**, 281–295 (2006).
34. S. A. Miller, C. T. Phare, Y.-C. Chang, X. Ji, O. Jimenez, A. Mohanty, S. Roberts, M. C. Shin, B. Stern, M. Zadka, and M. Lipson, "512-element actively steered silicon phased array for low-power LIDAR," in *Conference on Lasers and Electro-Optics* (OSA, 2018), paper JTh5C.2.

159.226.165.15 {ts '2021-04-27 02:22:43'}